Proceedings of the Seventh International Conference on
Railway Technology: Research, Development and Maintenance
Edited by: J. Pombo
Civil-Comp Conferences, Volume 15, Paper 7.4
Civil-Comp Press, Edinburgh, United Kingdom, 2026
ISSN: 2753-3239, doi: 10.4203/ccc.15.7.4

Physics-Informed Modelling of Particle-Size Effects on GPR Responses of Railway Ballast Using gprMax Simulations

L. Han[1,2], G. Jing[1], Y. Gao[1], S. Lu[1], L. Cheng[2] and H. Wang[3]

[1]School of Civil Engineering, Beijing Jiaotong University, China
[2]Engineering and Technology Institute Groningen, University of Groningen, Netherlands
[3]Baotou Railway Vocational&Technical College, China

Abstract

Ground penetrating radar (GPR) is widely used for railway ballast assessment, but the influence of ballast particle size on radar responses is still not sufficiently isolated and interpreted. This study investigates particle-size effects on GPR responses of single-size railway ballast using a simulation-based modelling framework built in gprMax. A simplified two-dimensional model was established, and representative ballast configurations with particle sizes of 20, 40, and 60 mm were generated under aligned geometric conditions with controlled porosity. Based on the simulated wavefield snapshots, A-scan responses, and geometry tensors, a physics-informed surrogate model was developed using a Time-Image architecture with additional A-scan supervision and light physics regularization. The results show that the proposed model can reconstruct representative wavefield patterns and receiver traces with useful accuracy while preserving key particle-size-dependent differences in early interface response, ballast-layer scattering, ballast-bottom response, and late-time signal behaviour. The study provides a practical proof-of-concept route for combining full-wave simulation and physics-informed surrogate modelling to analyse particle-size effects in railway ballast GPR responses.

Keywords: railway ballast, ground penetrating radar, particle-size effects, gprMax, physics-informed modelling, surrogate model.

1 Introduction

Ground penetrating radar, GPR, is widely used in railway infrastructure assessment because it can sense subsurface conditions without damaging the track structure [1,2]. In ballast-supported tracks, the received radar response is influenced by dielectric contrast, layer geometry, moisture, fouling, and particle arrangement [3]. Particle size matters in this context because it changes the internal heterogeneity of the ballast layer. That change affects wave scattering, interface-related reflections, and the late-time behaviour of the received signal [4]. A clearer description of particle-size-dependent radar responses can improve waveform interpretation and can support the development of faster digital analysis tools. The effect of particle size is still difficult to isolate in many ballast GPR studies. Field ballast is rarely controlled by one variable alone. Gradation, fouling, moisture, and structural complexity often vary at the same time. Many published studies focus on ballast condition assessment as a whole rather than on particle-size-dependent response mechanisms [5]. This leaves a gap between practical railway inspection and controlled electromagnetic interpretation. A simplified modelling framework is useful in this setting because it allows particle size to vary while the main structural conditions remain fixed.

Numerical simulation provides a practical way to build such a controlled framework. gprMax is a well-established full-wave solver for electromagnetic modelling based on the finite-difference time-domain method [6,7]. It has been used in many GPR studies because it can represent layered media, material contrasts, and antenna-driven wave propagation in a physically meaningful way. Railway ballast problems are particularly suitable for this route because the geometry can be parameterised and repeated under prescribed settings. Earlier work has already shown that GPR simulations and signal analysis can capture ballast-related geometric characteristics and ballast condition changes [8,9]. The main limitation is computational cost. Full-wave simulation is not convenient when repeated reconstruction or rapid comparative analysis is needed across many ballast configurations.

Surrogate modelling can reduce this cost, though a purely data-driven model may not preserve enough physical consistency when the target is a propagating electromagnetic field rather than a simple scalar output. Physics-informed learning offers a useful middle ground because it combines data supervision with constraints derived from governing equations [10]. This idea is relevant to ballast GPR because the wavefield is generated in a heterogeneous medium with known geometry and material parameters. A physics-informed surrogate model can therefore be used to reconstruct representative wavefield snapshots and receiver traces while still respecting the physical structure of the problem. Black-box and PINN-based surrogate modelling for railway-track GPR has also been explored in recent work at thesis and conference level [11,12]. Recent ballast-related studies have linked dielectric properties and geometric features to measurable GPR signatures [13]. Other studies have reported condition indicators, layer assessment results, and scattering-related observations that are also relevant to ballast response interpretation [14-17].

This study investigates particle-size effects on GPR responses of single-size railway ballast using gprMax simulations and a physics-informed surrogate modelling strategy. A simplified two-dimensional layered model is used to generate representative ballast configurations with particle sizes of 20 mm, 40 mm, and 60 mm under aligned geometric conditions and controlled porosity. On this basis, a surrogate model is constructed by combining a Time-Image architecture, A-scan supervision, and light physics regularization. The purpose of the model is not to replace full-wave simulation in a general sense. It is used here as a proof-of-concept tool for reconstructing representative wavefields and receiver responses, and for analysing how the response pattern changes with particle size. The rest of the paper introduces the numerical model and surrogate formulation, presents the particle-size-dependent response analysis, and discusses the reconstruction results obtained for representative simulated cases.

2 Methods

2.1 Numerical simulation model

The dataset was generated with gprMax, which solves electromagnetic wave propagation with the finite-difference time-domain method. A two-dimensional model was used in order to keep the geometry controllable and the computational cost acceptable for repeated comparative analysis. The model width was 1.50 m and the total height was 1.22 m. The vertical structure contained four layers. A 0.30 m ground layer was placed at the bottom. A 0.30 m air layer was placed above the ground. The ballast layer thickness was fixed at 0.30 m. A 0.30 m top air layer was placed above the ballast.

The transmitter and receiver were positioned at the same elevation, 0.30 m above the ballast surface. Their horizontal spacing was 0.20 m, and the antenna pair was centred at x = 0.75 m. The centre frequency was 2 GHz. The time window was 12 ns. The spatial step was fixed to 0.002 m in all directions. This produced an original field size of 610 x 750 cells for each snapshot frame. These stacks were downsampled to 203 x 250 by area interpolation before surrogate-model training. The automatically computed FDTD time increment for the present grid was about 4.72 ps. The original A-scan length was 2545 samples. A linear interpolation step was then used to resample the A-scan trace to 1024 samples. This setting is closer to the fixed sampling format commonly used in practical GPR acquisition systems. One A-scan was recorded at the receiver position for each simulated case. Eleven wavefield snapshots were stored at 2 ns, 3 ns, 4 ns, 5 ns, 6 ns, 7 ns, 8 ns, 9 ns, 10 ns, 11 ns, and 12 ns. These frames were used together with the receiver A-scan trace in the subsequent surrogate-model training stage.

2.2 Ballast geometry generation and dataset preparation

Three single-size ballast groups were considered, namely 20 mm, 40 mm, and 60 mm. Each group contained 1 simulated sample. The ballast particles were represented by equal-diameter circular inclusions in the two-dimensional section. A structured random-pruning strategy was used to generate the ballast layer. The procedure started from a staggered close-packed arrangement. A constrained random pruning step was then applied in order to introduce pores while keeping the support structure stable. The left and right margins were fixed at 1 cm. The ballast bottom was aligned with the lower ballast boundary. The ballast top was aligned across particle sizes, so that the layer thickness remained comparable when the particle diameter changed.

This controlled setting was adopted in order to separate particle-size-dependent effects from porosity-driven effects. The resulting dataset therefore contained 3 simulated cases in total. For each case, three data objects were retained. The first object was the receiver A-scan. The second object was the stack of 11 wavefield snapshots. The third object was the geometry tensor that stores local material properties. The geometry tensor contained four channels, namely relative permittivity, conductivity, relative permeability, and magnetic loss. In the present dry and non-magnetic configuration, the dominant contrast was the permittivity contrast between ballast and air, while the ground layer introduced an additional lower reflection interface.

2.3 Physics-informed surrogate model

The surrogate model was developed from the Time-Image model used in studies [11,12]. Several modifications were introduced for the present ballast problem. The model takes a scalar time value as input and predicts the two-dimensional Ez wavefield snapshot at that time. The input time is first encoded by a Fourier embedding with 16 frequencies and then passed through a multilayer perceptron with hidden widths of 128, 256, and 512. The resulting feature is reshaped into a compact latent tensor with 32 learned channels over a 13×16 grid. These channels are internal learned features rather than predefined physical variables. The decoder then converts this tensor into the final wavefield image. At each stage, bilinear interpolation is used to enlarge the feature map, and two 3×3 convolution layers with SiLU activations are used to refine it. Four decoding stages are used, so the spatial size grows from 13×16 to 26×32, 52×64, 104×128, and 208×256. A final interpolation adjusts the output to 203×250, and a 1×1 convolution produces the final Ez snapshot. These modifications improve the representation of oscillatory time variation, preserve spatial details during decoding, and make the model more suitable for joint reconstruction of wavefield snapshots and receiver traces in the present ballast problem.

The training objective combined wavefield reconstruction, receiver-trace supervision, and a light physics term. The total objective is given in Eq. (1).

$$L = L_{\mathrm{snap}} + \lambda_{\mathrm{a}} L_{\mathrm{a}} + \lambda_{\mathrm{p}} L_{\mathrm{phys}} \tag{1}$$

In Eq. (1), L is the total loss, L_{snap} is the snapshot reconstruction loss, L_{a} is the A-scan loss, L_{phys} is the physics residual loss, λ_{a} is the A-scan weight, and λ_{p} is the physics weight. The snapshot loss was defined as the mean squared error between the predicted and target normalized wavefield snapshots. A full-trace A-scan loss was still computed after each epoch for diagnosis. The final training configuration used λ_{a} =

0.1. The physics weight was set to λ_{p} = 1.0 in the final configuration. This does not mean that the physics term dominated the optimization. The residual was scaled by a factor of 1×10^{-28} before it was squared and averaged in order to keep the physics loss in a numerically stable range. The present formulation should therefore be interpreted as a light physics-guided regularization strategy.

The physics term was introduced as a light regularization rather than a dominant PINN constraint. The residual was based on a scalar damped wave equation with spatially varying material coefficients. The residual is written in Eq. (2).

$$r = u_{tt} - \frac{1}{\check{n}\mu}\left(u_{xx} + u_{zz}\right) + \frac{\sigma}{\check{n}} u_t \tag{2}$$

In Eq. (2), r is the partial differential equation (PDE) residual, u is the predicted Ez field, u_t and u_{tt} are the first and second temporal derivatives of u, u_{xx} and u_{zz} are the second spatial derivatives of μ along the horizontal and vertical directions, $\check{n}$ is the absolute permittivity, μ is the absolute permeability, and σ is the electrical conductivity.

The corresponding physics loss is given in Eq. (3).

$$L_{\mathrm{phys}} = \frac{1}{N}\sum_{i=1}^{N}\left(s_{\mathrm{r}} r_i\right)^2 \tag{3}$$

In Eq. (3), L_{phys} is the mean squared residual, N is the number of residual samples over the selected time instants and spatial cells, r_i is the residual at sample *i*, and s_{r} is a residual scaling factor.

Temporal derivatives in Eq. (2) were computed by Jacobian-vector products with respect to time. Spatial derivatives were computed on the image grid by second-order central finite differences. The discrete Laplacian used in the implementation is shown in Eq. (4).

$$\nabla^2 u \approx \frac{u_{i,j+1} - 2u_{i,j} + u_{i,j-1}}{\Delta x^2} + \frac{u_{i+1,j} - 2u_{i,j} + u_{i-1,j}}{\Delta z^2} \tag{4}$$

In Eq. (4), $\nabla^2 u$ is the discrete Laplacian of the predicted field, *j* denotes the horizontal x-index, *i* denotes the vertical z-index, $u_{i,j}$ is the field value at grid node *i*, *j*, Δx is the horizontal grid spacing, and Δz is the vertical grid spacing.

3 Results and Discussion

3.1 Simulated ballast geometries and particle-size-dependent responses

The generated ballast sections are shown in Figure 1. The three particle sizes preserve the same layer boundaries, the same top alignment, and the same target porosity. The geometric difference is therefore concentrated in the internal distribution of inclusions and voids. The 20 mm case contains many small particles and a finer-scale heterogeneity. The 40 mm and 60 mm cases contain fewer particles and larger local void regions. This change is visible in the sectional geometry alone, even before the radar response is examined. The fixed porosity setting is important here because it suppresses one major source of variation and makes the observed response differences easier to associate with particle size.

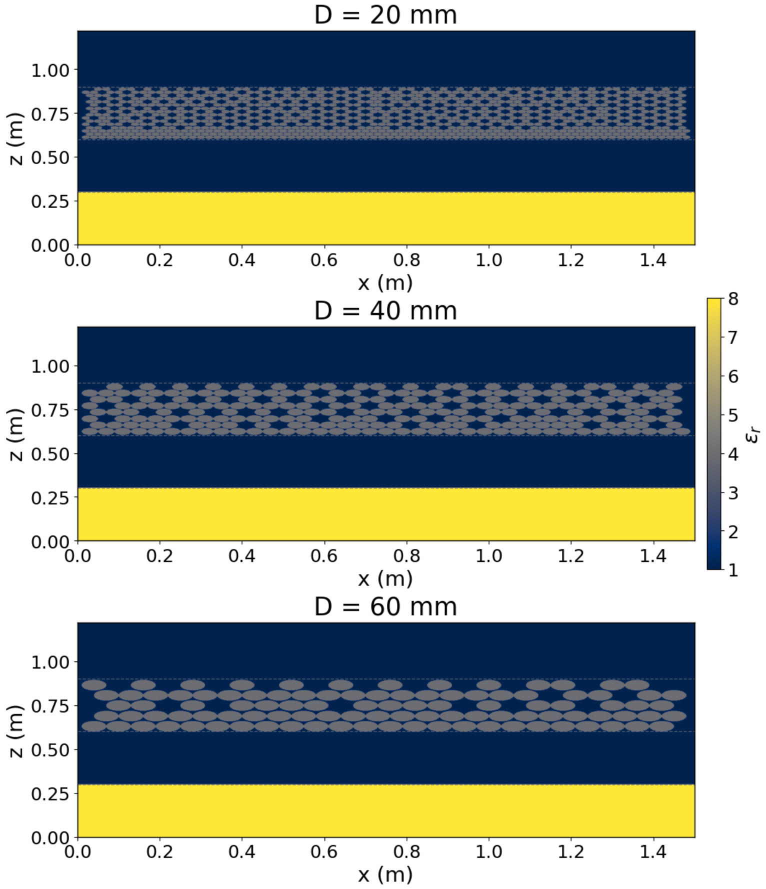

Figure 1: Generated single-size ballast geometries for particle sizes of 20 mm, 40 mm, and 60 mm.

The A-scan comparison across particle sizes is shown in Figure 2. The early part of the trace is very similar for the three cases. This behaviour is expected because the direct wave and the near-field air coupling are controlled mainly by the antenna geometry and the top air layer. The particle-size effect becomes clearer after the early wavelet. The envelope-guided interpretation suggests that the ballast-top-related response appears around 2.8 ns to 3.0 ns for all three particle sizes. The ballast-bottom-related response is broader and appears later, around 6.7 ns to 7.3 ns. The candidate air-ground response appears later still, in the approximate range from 8.2 ns to 9.3 ns. These windows should be treated as response zones rather than exact single-point picks because the model contains rough internal heterogeneity and the transmitter-receiver pair is offset by 0.20 m.

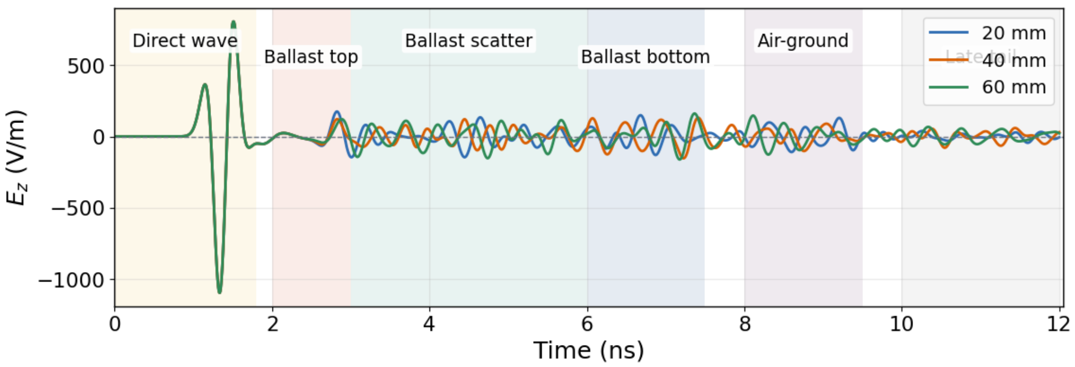

Figure 2: Comparison of simulated A-scan for different ballast particle sizes.

The envelope results provide a more stable view of the time-window behaviour, as shown in Figure 3. In the ballast-top window, the envelope peak is 182.18 V/m for D20, 122.27 V/m for D40, and 147.04 V/m for D60. In the ballast-scatter window, the envelope peak moves to 151.09 V/m for D20, 121.43 V/m for D40, and 154.12 V/m for D60. In the ballast-bottom window, the envelope peak becomes 151.88 V/m for D20, 160.41 V/m for D40, and 171.85 V/m for D60. This pattern indicates that the largest particle size does not always give the strongest early local peak, though it tends to produce a stronger late response in the lower part of the ballast-related signal. The D20 case also shows a pronounced local peak in the 3 ns to 6 ns interval. That feature should not be interpreted as stronger overall scattering by itself. It is more consistent with a stronger local coherent contribution, while the D60 case distributes more energy over a wider oscillatory interval.

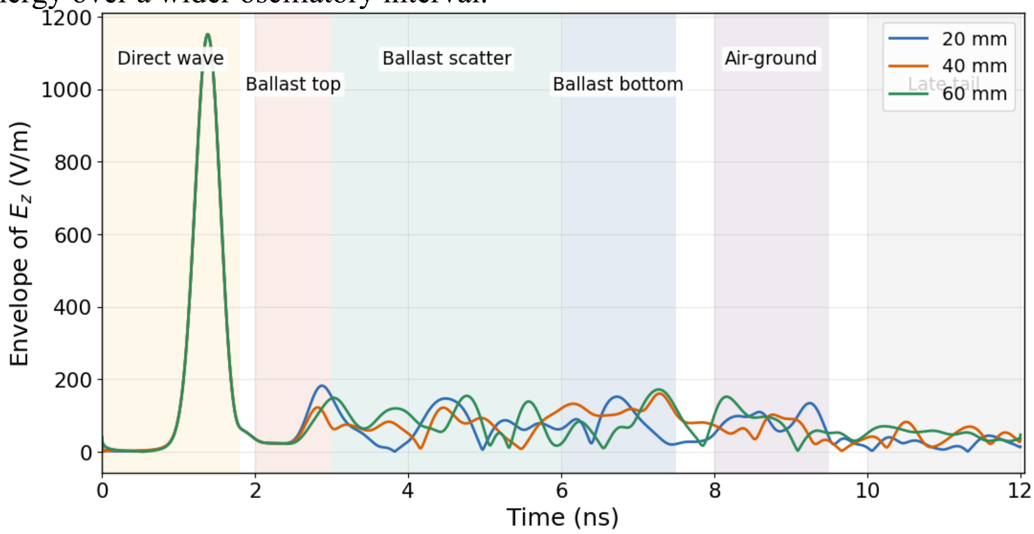

Figure 3: Envelope comparison of simulated A-scan for different ballast particle sizes.

3.2 Surrogate-model reconstruction performance

The physics-informed surrogate model was evaluated on one representative case from each particle-size group. The reported metrics therefore describe reconstruction quality for the simulated case used in training, which is consistent with the proof-of-concept scope of the present study. The best-performing setup used a learning rate of 2×10-4, a weight decay of 1×10-6, 16 Fourier frequencies, 80 fine-tuning epochs, and GPU-based training. The model was warm-started from a previously trained Time-Image checkpoint, then refined with the 1024-point A-scan setting and the light physics term described above. The loss curves show the same overall behaviour, as shown in Figure 4. The stable total loss decreases during training and then approaches a plateau. The plateau is reached after about 45 epochs for D20, 65 epochs for D40, and 51 epochs for D60.

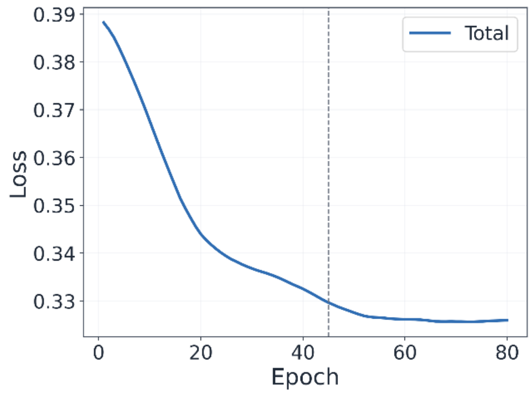

(a)

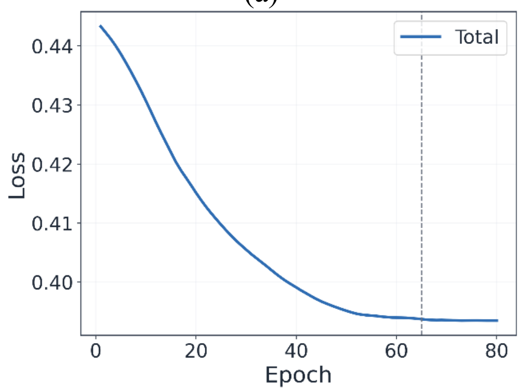

(b)

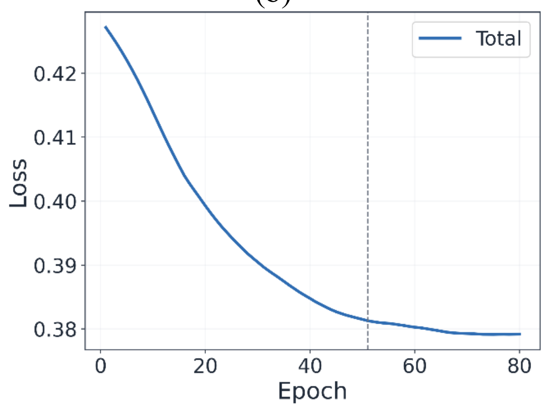

(c)

Figure 4: Total training loss for different ballast particle sizes: (a) 20 mm, (b) 40 mm, (c) 60 mm.

The selected snapshot-frame metrics show the same pattern, as shown in Figure 5. In the early frame at 2 ns, the model performs very well for all three particle sizes, with R^2 values above 0.92. The quality drops at 7 ns, where scattering and lower-interface interactions are stronger. The quality drops further at 12 ns, where the late-time tail is weaker and more diffuse. This behaviour is physically sensible. The early field is dominated by strong and coherent structures. The later field is more sensitive to internal heterogeneity and small phase differences. The surrogate model still captures the main field topology in the later frames, though the predicted late-time amplitude becomes smoother than the simulated reference.

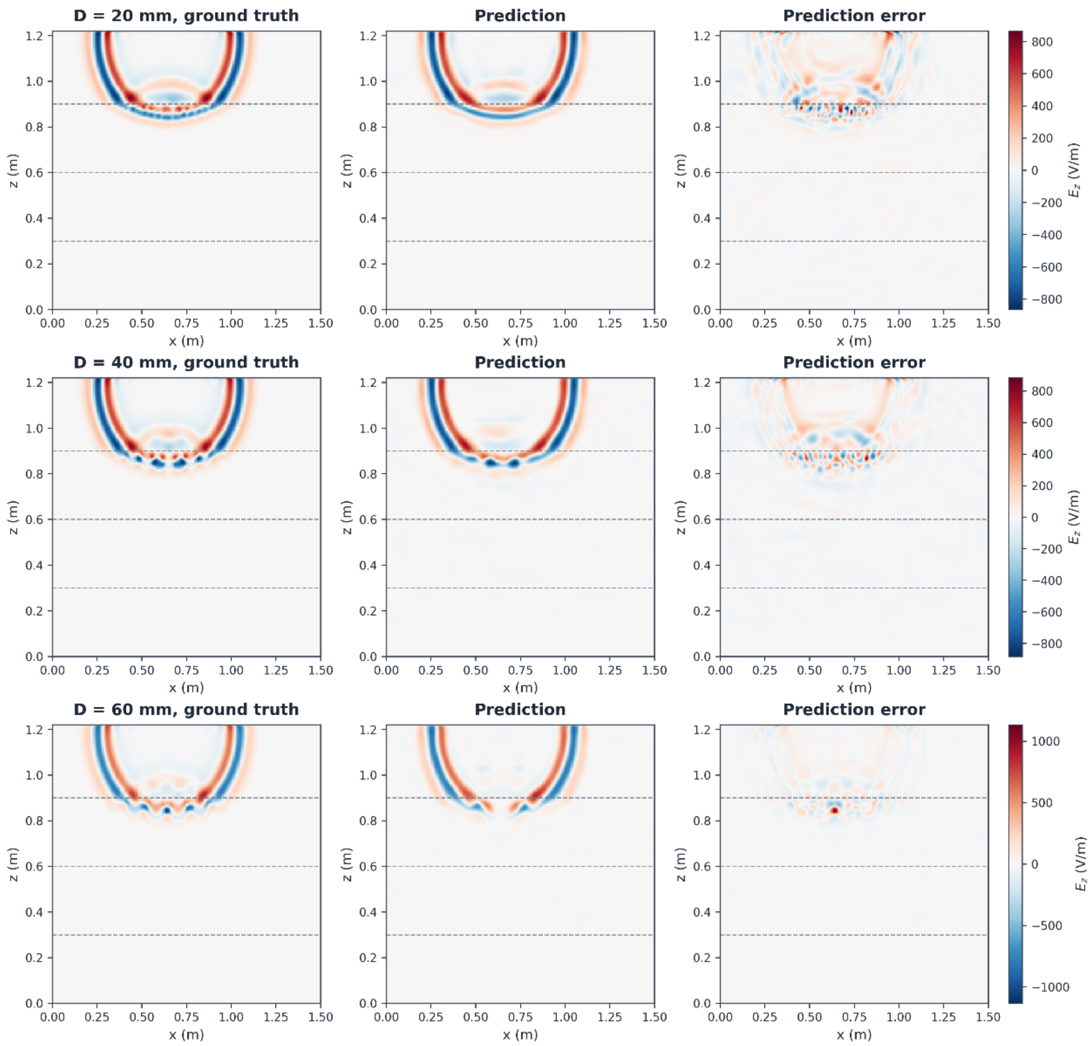

(a)

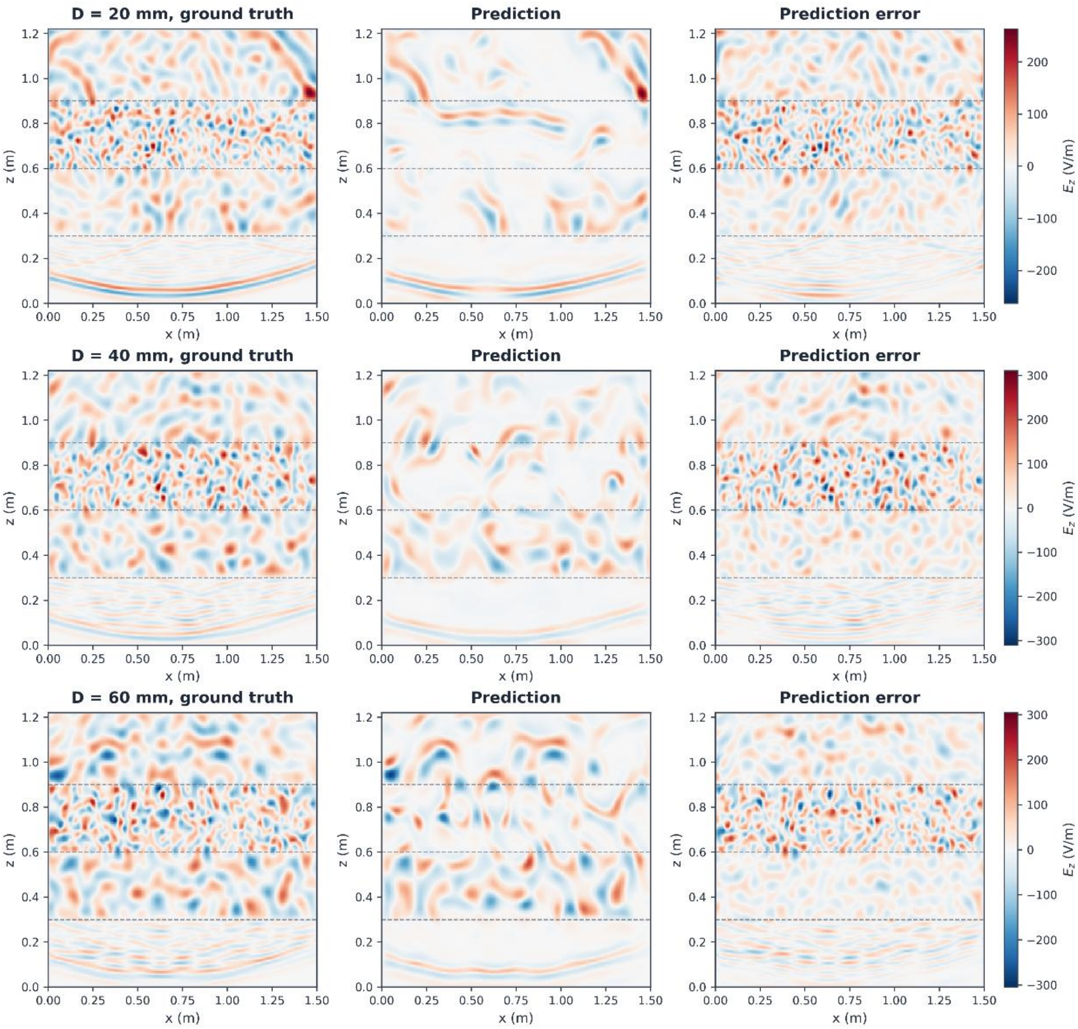
D = 20 mm, ground truth
Prediction
Prediction error
D = 40 mm, ground truth
Prediction
Prediction error
D = 60 mm, ground truth
Prediction
Prediction error
z (m)
x (m)
E_z (V/m)

(b)

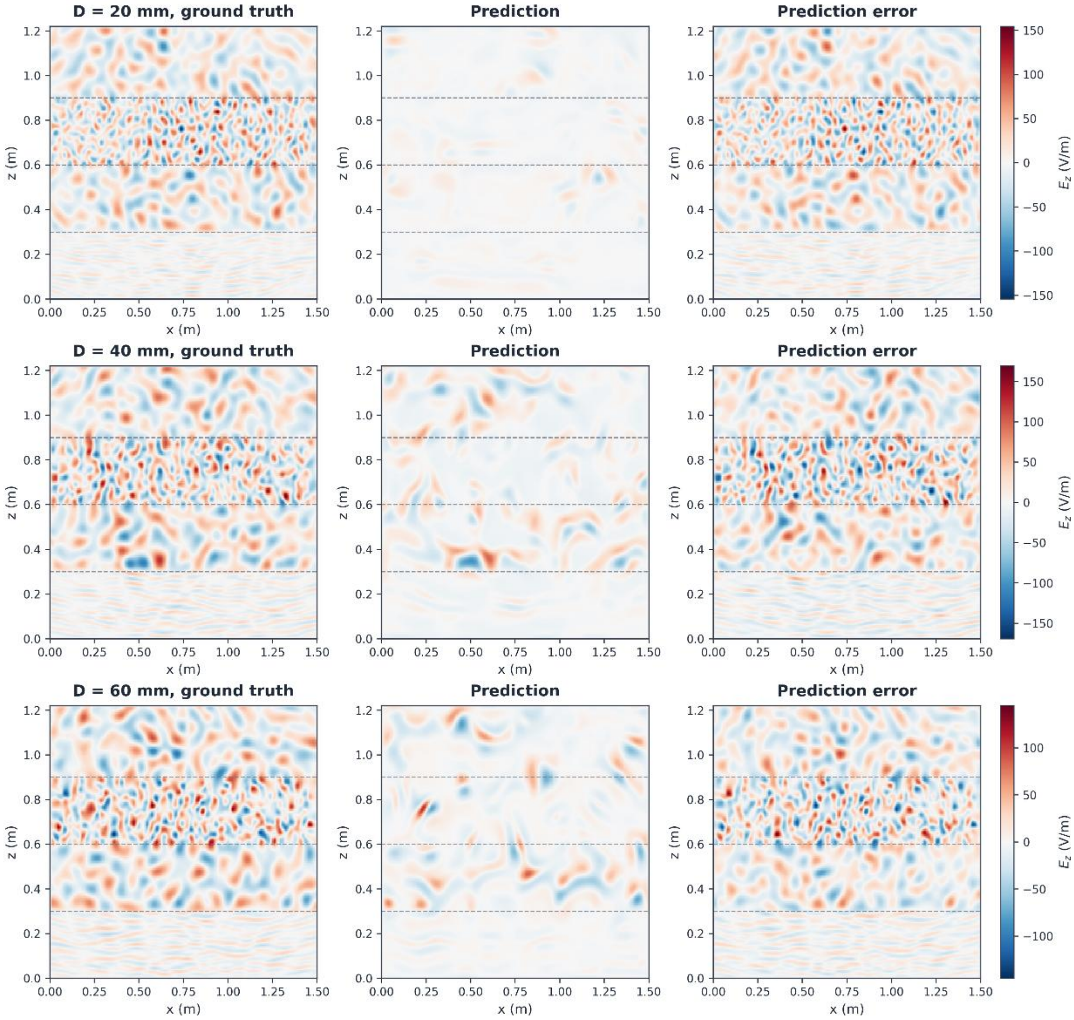

(c)

Figure 5: Wavefield reconstruction results for different ballast particle sizes: (a) t=2 ns, (b) t=7 ns, (c) t=12 ns,

Table 1 summarises the main results. These results show two consistent tendencies. The first tendency is that the receiver-trace reconstruction is easier than full-field reconstruction under the present setup. The second tendency is that the relative ranking of particle sizes is not identical for the two tasks. D40 gives the strongest A-scan result, while D20 gives the strongest overall snapshot result. This difference is reasonable because the A-scan objective focuses on one receiver location, while the snapshot objective covers the complete wavefield over the whole spatial domain. The model can therefore fit the local receiver trace very well even when some distributed field details remain harder to reconstruct.

Group	Best epoch	Snapshot R^2	Snapshot RMSE	A-scan R^2	A-scan RMSE
D20 mm	45	0.74	33.86	0.86	51.74
D40 mm	65	0.66	39.20	0.88	47.89
D60 mm	51	0.68	38.64	0.86	50.92

Table 1: Surrogate-model performance for different ballast particle sizes.

4 Conclusions and Contributions

This paper examined particle-size effects on simulated GPR responses of single-size railway ballast and developed a physics-informed surrogate modelling strategy for representative reconstruction tasks. The main conclusions are as follows.

- Under the controlled conditions used in this study, particle size changed both the internal ballast geometry and the simulated GPR response. The earliest part of the A-scan was dominated by the direct wave, while clearer particle-size-dependent differences appeared in the later ballast-related windows. A combined reading of A-scan windows, signal envelopes, and snapshot fields was more reliable than interpreting isolated peaks from the raw A-scan trace alone.
- The proposed Time-Image surrogate model, combined with A-scan supervision and a light physics constraint, reconstructed representative responses with useful accuracy for all three particle-size cases. The snapshot reconstruction R^2 values were 0.74 for 20 mm, 0.66 for 40 mm, and 0.68 for 60 mm. The corresponding A-scan R^2 values were 0.86, 0.88, and 0.86.
- The light physics term improved the balance between wavefield reconstruction and receiver-trace reconstruction under the present setting. This result supports the use of the proposed framework as a proof-of-concept route for particle-size-dependent ballast GPR analysis, rather than as a broad generalization benchmark.

Future work will extend the present framework to additional samples, broader particle-size ranges, and more realistic ballast configurations. A further step will be to test the current surrogate formulation on larger datasets and examine its stability in cross-case prediction.

Acknowledgements

The authors gratefully acknowledge the support provided by the Fundamental Research Funds for the Central Universities of China (2025YJS100), the Natural Science Foundation of Inner Mongolia Autonomous Region (2022QN05033) and the Program of China Scholarship Council (202507090043).

References

[1] H.M. Jol, "Ground Penetrating Radar Theory and Applications", Elsevier, Amsterdam, Netherlands, 2008.

[2] S. Wang, Y. Guo, G. Liu, G. Jia, Q. Fang, H. Liu, "State-of-the-art review of ground penetrating radar applications for railway ballast inspection", Sensors, 22(7), 2450, 2022. doi:10.3390/s22072450

[3] M. Silvast, A. Nurmikolu, B. Wiljanen, M. Levomaki, "An inspection of railway ballast quality using ground penetrating radar in Finland", Proceedings of the Institution of Mechanical Engineers, Part F: Journal of Rail and Rapid Transit, 224(5), 345-351, 2010. doi:10.1243/09544097JRRT367

[4] L. Bianchini Ciampoli, F. Tosti, M.G. Brancadoro, F. D'Amico, A.M. Alani, A. Benedetto, "A spectral analysis of ground-penetrating radar data for the assessment of the railway ballast geometric properties", NDT and E International, 90, 39-47, 2017. doi:10.1016/j.ndteint.2017.05.005

[5] A. Benedetto, F. Tosti, L. Bianchini Ciampoli, A. Calvi, M.G. Brancadoro, A.M. Alani, "Railway ballast condition assessment using ground-penetrating radar: An experimental, numerical simulation and modelling development", Construction and Building Materials, 140, 508-520, 2017. doi:10.1016/j.conbuildmat.2017.02.110

[6] C. Warren, A. Giannopoulos, I. Giannakis, "gprMax: Open source software to simulate electromagnetic wave propagation for ground penetrating radar", Computer Physics Communications, 209, 163-170, 2016. doi:10.1016/j.cpc.2016.08.020

[7] A. Giannopoulos, "Modelling ground penetrating radar by GprMax", Construction and Building Materials, 19(10), 755-762, 2005. doi:10.1016/j.conbuildmat.2005.06.007

[8] S.S. Artagan, V. Borecky, "Advances in the nondestructive condition assessment of railway ballast: A focus on GPR", NDT and E International, 115, 102290, 2020. doi:10.1016/j.ndteint.2020.102290

[9] F. Tosti, L. Bianchini Ciampoli, A. Calvi, A.M. Alani, A. Benedetto, "An investigation into the railway ballast dielectric properties using different GPR antennas and frequency systems", NDT and E International, 93, 131-140, 2018. doi:10.1016/j.ndteint.2017.10.003

[10] M. Raissi, P. Perdikaris, G.E. Karniadakis, "Physics-informed neural networks: A deep learning framework for solving forward and inverse problems involving nonlinear partial differential equations", Journal of Computational Physics, 378, 686-707, 2019. doi:10.1016/j.jcp.2018.10.045

[11] T. Rigoni, "Railway infrastructure GPR dataset creation and modeling via black box and physics-informed neural networks", Master Thesis, ETH Zurich, Zurich, Switzerland, 2024.

[12] T. Rigoni, G. Arcieri, M. Haywood-Alexander, D. Haener, E. Chatzi, "Modeling GPR observations on railway tracks via black box and physics informed neural networks", in "Proceedings of the 9th European Congress on Computational Methods in Applied Sciences and Engineering, ECCOMAS

Congress 2024", International Centre for Numerical Methods in Engineering, Barcelona, Spain, paper 244, 2024. doi:10.23967/eccomas.2024.244
[13] L. Bianchini Ciampoli, A. Calvi, F. D'Amico, "Railway ballast monitoring by GPR: A test-site investigation", Remote Sensing, 11(20), 2381, 2019. doi:10.3390/rs11202381
[14] F.N. Birhane, Y.T. Choi, S.J. Lee, "Development of condition assessment index of ballast track using ground-penetrating radar, GPR", Sensors, 21(20), 6875, 2021. doi:10.3390/s21206875
[15] Y. Guo, S. Wang, G. Jing, F. Yang, G. Liu, W. Qiang, Y. Wang, "Assessment of ballast layer under multiple field conditions in China", Construction and Building Materials, 340, 127740, 2022. doi:10.1016/j.conbuildmat.2022.127740
[16] A. Borkovcova, V. Borecky, S.S. Artagan, F. Sevcik, "Quantification of the mechanized ballast cleaning process efficiency using GPR technology", Remote Sensing, 13(8), 1510, 2021. doi:10.3390/rs13081510
[17] L. Liu, Z. Li, S. Arcone, L. Fu, Q. Huang, "Radar wave scattering loss in a densely packed discrete random medium: Numerical modeling of a box-of-boulders experiment in the Mie regime", Journal of Applied Geophysics, 99, 68-75, 2013. doi:10.1016/j.jappgeo.2013.08.022